Research Article | Vol. 32, No. 17 / 12 Aug 2024 / Optics Express 29887
Optics EXPRESS

Fiber optic relative humidity and temperature sensor with the cascaded Vernier effect based on the C-shaped cavity structure

KE ZHAO,[1] BOJUN SONG,[1] CANJIA YE,[1] XUEMEI JIN,[2,3,6] CHANGYUAN YU,[4] GUIYAO ZHOU,[1] JINGSHUN PAN,[1,4,5,7] AND XUGUANG HUANG[1,8]

[1]*Guangdong Provincial Key Laboratory of Nanophotonic Functional Materials and Devices, South China Normal University, Guangzhou 510006, China*
[2]*Guangzhou Marine Geological Survey, China Geological Survey, Guangzhou 510075, China*
[3]*Gas Hydrate Engineering Technology Center, China Geological Survey, Guangzhou 510075, China*
[4]*Department of Electronic and Information Engineering, The Hong Kong Polytechnic University Kowloon, Hong Kong 999077, China*
[5]*School of Electronics and Information Technology, Guangdong Provincial Key Laboratory of Optoelectronic Information Processing Chips and Systems, Sun Yat-sen University, Guangzhou 510275, China*
[6]*2018010236@m.scnu.edu.cn*
[7]*20230034@m.scnu.edu.cn*
[8]*huangxg@scnu.edu.cn*

Abstract: The water-absorbent sensing film, coated on the surface of traditional optical fiber humidity sensors, often suffers from detachment issues. In this paper, we present what we believe to be a new fiber-optic cascaded Fabry-Perot interferometer sensor for detecting relative humidity (RH) and temperature, without the need for sophisticated instrumentation. The sensing structure comprises two sections of single-mode optical fibers and a C-shaped cavity between them. The C-shaped cavity is created by grinding the side of a hollow-core fiber with fiber optic abrasive paper. The Vernier effect arises from the cascaded interaction between the C-shaped cavity filled with ultraviolet optical glue (NOA61) and the subsequent single-mode fiber pigtail. The sensor exhibits a high RH sensitivity of 0.248 nm/%RH (35-95%RH) and an RH resolution of up to 0.08%RH. It also has high-temperature sensitivities of -1.091 nm/°C (25 - 65°C). Furthermore, simultaneous measurement of RH and temperature is achieved by establishing a dual parameter matrix, and the sensor's response time and recovery time for RH and temperature are within 300s. Therefore, this work provides a simple and cost-effective manufacturing process and the proposed RH and temperature sensor features a compact size, strong environmental adaptability, and significant potential for practical applications.

1. Introduction

Relative humidity (RH) and temperature are the most basic physical parameters, significantly influencing both our human life and productive activities. For instance, to preserve human health, it is recommended that the indoor temperature be maintained within a range of 20°C to 30°C and a relative humidity of 30% to 80% RH [1–3]. In addition, RH and temperature monitoring are of paramount importance in various fields, such as the operation of integrated circuits, food processing and storage, performance testing of manned spacecraft, and agricultural cultivation and breeding, etc. Currently, commercial sensors for monitoring RH and temperature are mainly capacitive or resistive devices [4]. However, with the expansion of application areas, the requirements for detection accuracy and resistance to complex environments are increasing, and these electronic devices have difficulties operating in complex environments, such as corrosive

#534287 https://doi.org/10.1364/OE.534287
Journal © 2024 Received 1 Jul 2024; revised 20 Jul 2024; accepted 22 Jul 2024; published 2 Aug 2024

Optics EXPRESS

media, confined spaces, underwater ocean monitoring and strong electromagnetic interference [5]. In contrast, fiber-optic sensors possess numerous advantages such as high sensitivity, small size, and resistance to electromagnetic interference, enabling remote, real-time, and online monitoring in extremely harsh environments [6–8]. At present, the reported fiber-optic RH and temperature sensors can be primarily classified into several types based on their sensing structures: Mach-Zehnder interferometer (MZI) [9,10], Michelson interferometer (MI) [11,12], Fabry-Perot interferometer (FPI) [13–15], Sagnac interferometer (SI) [16], fiber Bragg grating (FBG) [17–19], long-period grating (LPG) [20], and surface plasmon resonance (SPR) [21], etc. Among them, FPIs have garnered significant attention from researchers owing to their merits, including cost-effective production, straightforward design, and convenient inspection [22]. Meanwhile, in Ref. [22], the detection principle of optical fiber FPI sensor is explained in detail and several manufacturing methods of diaphragm-based optical fiber FPI sensor on are summarized.

Nowadays, most fiber optic RH and temperature sensors are fabricated by coating a water-absorbent sensing film directly onto the sensing end face or side to achieve RH and temperature detection. However, the thickness and uniformity of the sensing film coated on these sensors are difficult to control. After a period of use, the sensing film may partially peel off, resulting in detection failure. Moreover, traditional humidity-sensitive materials such as polyvinyl alcohol (PVA) typically possess high hygroscopicity and expansive properties [9,23]. As a result, they are prone to undergoing hydrolysis in high-humidity environments and to experiencing drying shrinkage and warping in low-humidity environments, significantly limiting the application range of these sensors.

The optical Vernier effect (OVE) has emerged as an effective means to improve the detection performance of fiber-optic sensors [24,25]. Optical fiber sensors utilizing the OVE, typically feature two interferometric structures (commonly two FPIs with closely similar cavity lengths) [26]. When the free spectral ranges (FSRs) generated by these two interferometric structures are close, the spectral overlap forms a Vernier envelope. Compared to a single FPI, measuring the shift of the Vernier envelope can greatly enhance the corresponding detection sensitivity of the sensor, even several orders of magnitude higher [27–29].

In this work, we propose a fiber optic RH and temperature sensor utilizing a remarkably simple fabrication process. Based on a structure of single-mode fiber (SMF) – hollow-core fiber (HCF) – single-mode pigtail, an open C-shaped cavity is created by grinding one side of the hollow-core fiber using a fiber abrasive paper. Then, a sensitive material, NOA 61, is injected into this sensing cavity to detect external environmental changes, simultaneously forming a Vernier effect with subsequent reference cavity. The experimental results show that the sensor has a RH sensitivity of 0.248 nm/%RH, with a resolution of 0.08%RH in the range of 35%RH to 95%RH, and its temperature sensitivity is -1.091 nm/°C in the range of 25-65°C. Moreover, the sensor's RH response/recovery times are 300s/270s, while for temperature, they are 210s/240s. Both are under 300s. Meanwhile, by measuring the change of optical signal in the reflection spectrum, simultaneous measurement of RH and temperature has been achieved. Finally, the proposed sensor exhibits exceptional environmental endurance and a broad range of RH and temperature measurement due to the strong antioxidant and anti-corrosion capabilities of NOA61.

2. Sensor detail

2.1. Sensing principle

Figure 1 shows the structure of the optical fiber RH and temperature sensor. The sensor structure consists of a single-mode fiber 1 (SMF1), a hollow-core fiber (HCF) segment of several hundred micrometers, and a similarly sized single-mode fiber 2 (SMF2) pigtail, forming a compact cascaded Fabry-Perot (FP) fiber structure. By grinding a side of the hollow-core fiber, a C-shaped cavity is formed, which is then filled with an ultraviolet (UV) curing optical glue to sense the

Optics EXPRESS

external environment. The two ends of the C-shaped cavity constitute reflective surfaces M1 and M2 with SMF1 and SMF2, respectively. The tail end of SMF2 forms a reflective surface M3 with external air.

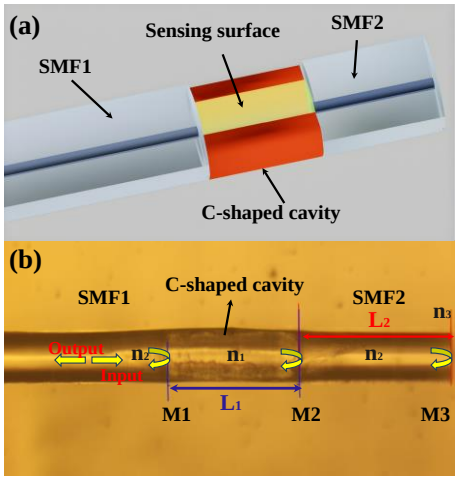

Fig. 1. (a) Schematic diagram of the sensor. (b) Physical image of the structure.

This configuration is directly spliced by two Fabry-Perot Interferometer (FPI) structures, effectively forming three FPIs of varying lengths: two short ones (FPI1 and FPI2) and a longer one (FPI3). The three reflective surfaces primarily generate three reflected light beams, and thus the compact cascaded Fabry-Perot (FP) fiber structure can be regarded as a three-beam interference model. Finally, the total reflected light field intensity of the sensor is [30,31]:

$$\begin{aligned} E_{re} = E_0[&\sqrt{R1} + (1-\alpha 1)(1-R1)\sqrt{R2}e^{-j2\phi 1} + \\ &(1-\alpha 1)(1-R1)(1-\alpha 2)(1-R2)\sqrt{R3}e^{-j2(\phi 1+\phi 2)}], \end{aligned} \tag{1}$$

where E_0 is the incident light field, and R_1, R_2, and R_3 are the reflectances of the three reflective surfaces, respectively. $\alpha 1$ and $\alpha 2$ are the transmission loss rates, and ϕ_1 and ϕ_2 are the optical round-trip phase differences of FPI1 and FPI2, respectively, which can be expressed as:

$$\begin{aligned} \phi_1 &= 2\pi n_1 L_1/\lambda, \\ \phi_2 &= 2\pi n_2 L_2/\lambda, \end{aligned} \tag{2}$$

where n_1, n_2, and n_3 represent the refractive indices of the core of the single-mode optical fiber, UV glue, and air, respectively. L_1, L_2, and L_3 ($L_3 = L_1 + L_2$) refer to the respective cavity lengths of FPI1, FPI2, and FPI3. According to the Fresnel reflection principle, R_1, R_2, and R_3 can be expressed as:

$$\begin{aligned} R_1 = R_2 &= (n_1 - n_2)^2/(n_1 + n_2)^2, \\ R_3 &= (n_0 - n_1)^2/(n_0 + n_1)^2. \end{aligned} \tag{3}$$

The light intensity I_1, I_2, and I_3 of the three reflected lights at the reflecting surface M1, M2, M3, and M4 are respectively:

$$\begin{aligned} I_1 &= R_1|E_0|^2, \\ I_2 &= (1-\alpha_1)^2(1-R_1)^2R_2|E_0|^2, \\ I_3 &= (1-\alpha_1)^2(1-R_1)^2(1-\alpha_2)^2(1-R_2)^2R_3|E_0|^2. \end{aligned} \tag{4}$$

Optics EXPRESS

Thus, the light intensity I_{re} of the total reflected light can be expressed as [32]:

$$I_{re} = I_{re} = I_1 + I_2 + I_3 + 2\sqrt{I_1 I_2}\cos(2\phi_1) + 2\sqrt{I_2 I_3}\cos(2\phi_2) + 2\sqrt{I_1 I_3}\cos[2(\phi_1 + \phi_2)]. \tag{5}$$

It can be observed that the first and second cosine functions are caused by the reflected light intensity of FPI1 and FPI2, respectively, and the third cosine function is caused by the reflected light intensity of FPI3 after combination. In Eq. (5), if the frequency of the first and second cosine terms is very close, an optical beat frequency will be generated. The envelope of this optical beat is known as the Vernier envelope, and the third cosine term will serve as the fine internal fringes within this envelope [33]. Based on the beat frequency formula, the cosine function representing the envelope is:

$$A\cos(2\phi_1 - 2\phi_2) = A\cos\left[\frac{2\pi(2n_1L_1 - 2n_2L_2)}{\lambda}\right], \tag{6}$$

where A represents the amplitude intensity of the envelope. Based on the free spectral range (FSR) of a single FPI ($FSR = \lambda^2/2nL$), the FSR of the Vernier envelope can be derived as [28]:

$$\mathrm{FSR}_{envelope} = \left|\frac{\lambda^2}{2n_1L_1 - 2n_2L_2}\right| = \lambda^2\left|\frac{\frac{1}{4n_1L_1n_2L_1}}{\frac{1}{2n_1L_1} - \frac{1}{2n_2L_2}}\right| = \frac{\mathrm{FSR}_1\mathrm{FSR}_2}{|\mathrm{FSR}_2 - \mathrm{FSR}_1|}, \tag{7}$$

where FSR_1 and FSR_2 are the free spectral ranges of FPI1 and FPI2 respectively. When FPI1 is used as the sensing cavity and the optical path length of FPI1 is slightly greater than that of FPI2, due to the Vernier effect, the cascaded response sensitivity can be amplified by a factor of M, where M can be expressed as [33]:

$$\mathrm{M} = \frac{\mathrm{FSR}_{envelope}}{\mathrm{FSR}_1} = \frac{\mathrm{FSR}_2}{|\mathrm{FSR}_2 - \mathrm{FSR}_1|} = \frac{1}{|\frac{n_1L_1}{n_2L_2} - 1|}, \tag{8}$$

It can be seen that M is determined by the ratio of the optical path lengths of FPI1 and FPI2. When $\mathrm{FSR}_1 > \mathrm{FSR}_2$ (i.e., $n_1L_1 < n_2L_2$), the drift direction of the vernier spectral envelope is opposite to that of the fine fringes within the vernier spectrum. Conversely, When $\mathrm{FSR}_1 < \mathrm{FSR}_2$ (i.e., $n_1L_1 > n_2L_2$), the drift directions are the same. According to Eq. (6), when $2\phi_1$ - $2\phi_2 = 2m\pi$, the peak wavelength λ_m of the envelope can be derived:

$$\lambda_m = \frac{2(n_1L_1 - n_2L_2)}{m}, \tag{9}$$

where m represents the order of the interference peak. When the RH changes, only the refractive index of the FPI1 cavity varies. Therefore, the humidity sensitivity of the sensor can be expressed as:

$$S_{\mathrm{FSR},H} = \frac{\partial\lambda_m}{\partial RH} = \mathrm{M}\lambda_m\frac{1}{n_1}\frac{\partial n_1}{\partial RH}. \tag{10}$$

When the ambient temperature T changes, due to the thermos-optic effect and thermal expansion effect, the refractive index and length of FPI1 and FPI2 cavities will change. However, the thermos-optic coefficient and thermal expansion coefficient ($\sim 10^{-6}$) of the optical fiber are far less than those of most temperature and RH sensitive materials ($\sim 10^{-4}$) [34]. Thus, the temperature sensitivity of the sensor is:

$$S_{\mathrm{FSR},T} = \frac{\partial\lambda_m}{\partial T} = \mathrm{M}\lambda_m\left(\frac{1}{n_1}\frac{\partial n_1}{\partial T} + \frac{1}{L_1}\frac{\partial L_1}{\partial T}\right) = \mathrm{M}\lambda_m(\alpha + \beta), \tag{11}$$

where α and β represent the thermo-optic coefficient and thermal expansion coefficient of the sensitive material, respectively.

Optics EXPRESS

2.2. Simulation analysis

MATLAB software is used to perform simulation analysis of the spectral characteristics of this sensing structure. As shown in Fig. 2(a), we can observe that the longer the sensing cavity, the greater the transmission loss becomes. Consequently, it is recommended to shorten the length of the sensing cavity as much as possible, preferably not exceeding 500 µm. Furthermore, as demonstrated in Table 1, it can be concluded that when the FP cavity length is maintained at a 1:1 ratio, an increase in the cavity length does not alter the magnification factor M, but it leads to a reduction of the free spectral range (FSR) of the Vernier envelope. Since the broadband light source operates within the C + L band (1520 nm – 1620 nm), which limits the experimental detection range, the FSR of the Vernier envelope is not suitable to be excessively large. Therefore, the lengths of the sensing cavity and the reference cavity can be selected as 400um respectively. Then, based on Eq. (7), it is theoretically not advisable to make the optical path difference ($|n_1L_1 - n_2L_2|$) of the two FP cavities too small, as this would also result in an excessively large FSR of the envelope, potentially exceeding the measurement range and consequently losing the amplification effect. Therefore, we can appropriately reduce the length of L_1 and increase the length of L_2 to achieve a suitable envelope spectral FSR, which is approximately 20 nm. Based on the above discussion, we select a length of 350 µm for FPI1 and a length of 420 µm for FPI2 for the conduct of subsequent experimental investigations.

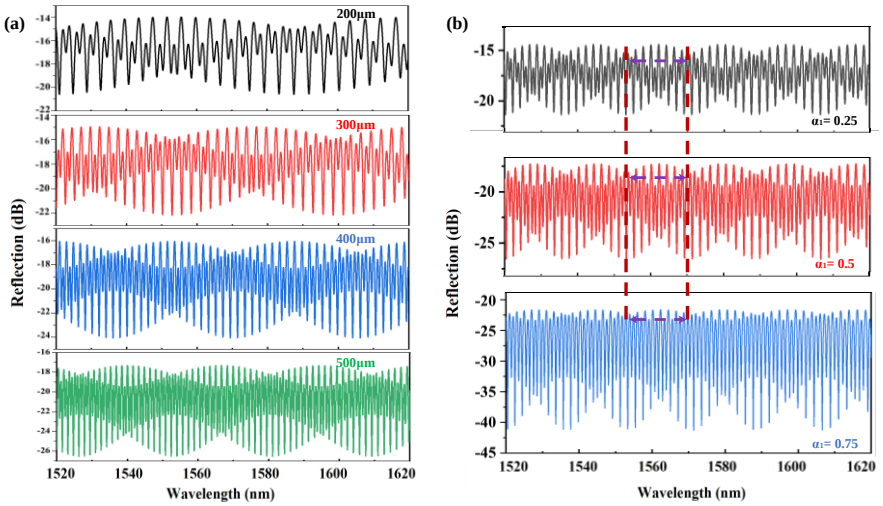

Fig. 2. (a) and (b): Simulated spectra of varying FP cavity lengths and losses.

Table 1. MATLAB simulated spectral data

FP cavity length (µm)	Magnification (M)	Envelope FSR (nm)
200	16.3	67.3
300	16.3	44.8
400	16.3	33.6
500	16.3	26.9

Next, assuming the lengths of two FP cavities are $L_1 = 350$ µm and $L_2 = 400$ µm, and that the loss rate α_1 takes values of 0.25, 0.5, and 0.75, it can be seen that as α_1 increases, the light intensity of the Vernier spectrum decreases, while it does not affect the FSR of the Vernier envelope (Fig. 2(b)). Furthermore, as α_1 increases, the contrast of the lower envelope of the

Optics EXPRESS

Vernier spectrum becomes higher. However, the presence of background noise can impact the extraction of the lower envelope and the subsequent fitting process, leading to distortions in the fitting results.

2.3. Sensor fabrication

The fabrication steps of the sensor, including structure cutting and welding, are shown in Fig. 3(a). The 8.2/125 μm single-mode fiber (SMF) is from Yangzi Corp., Ltd., and the 75/125 μm hollow-core fiber (HCF) is from Zhengzhou Inno Hi-Tech Co., Ltd. To prevent excessive fusion, the discharge intensity and discharge time of the optical fiber splicer FITEL S178 are set to 10 units and 500 ms, respectively. In addition, Fig. 3(b) presents the cleaving platform with an accuracy of 10 μm, and the HCF and the SMF are cut to 350 μm and 420 μm, respectively. Based on above steps, the splicing of the SMF-HCF-SMF structure is completed.

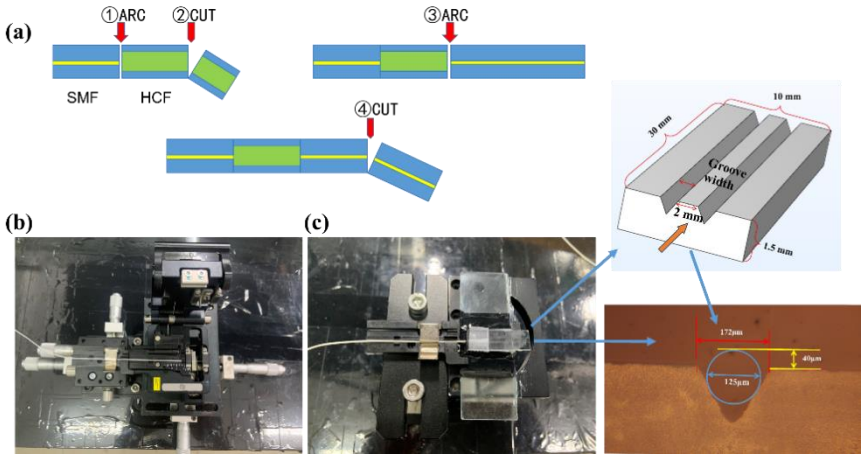

Fig. 3. sensor manufacturing process: (a) Splicing of SMF-HCF-SMF structure. (b) Cleaving platform. (c) Abrasive platform and dual-channel fiber array V-groove.

To obtain the C-shaped cavity in the structure, directly purchasing C-shaped optical fibers is not only expensive, but also difficult to process with ordinary fiber-cutting tools. On the other hand, using femtosecond laser equipment for modification would significantly increase the cost. In fact, there does exist a simpler and easier preparation method to obtain the C-shaped cavity. By using diamond abrasive paper, the side of the HCF in the V-groove can be ground away to form a C-shaped cavity. This method not only has a simple manufacturing process and low cost, but also ensures the splicing and cutting quality of the optical fiber. Moreover, with a cladding thickness of only 25 μm, the HCF is fragile and prone to breakage during grinding. Therefore, selecting the right diamond abrasive paper is key. After many tests, we found the D15 diamond abrasive paper (1200 grit, 15 μm particles) most effective for fabricating the C-shaped cavity.

The prepared SMF-HCF-SMF structure is fixed in the 3 cm dual-channel fiber array V-groove of the abrasive platform. As shown in Fig. 3(c), the V-groove effectively limits the grinding depth of the HCF to no more than 40 μm, preventing excessive grinding and ensuring structural stability. The C-shaped cavity formed by HCF has been successfully and stably obtained many times through proper grinding. Figure 4(a) shows the image of the compact cascaded FP fiber structure, which is manufactured according to the specifications of 350 μm HCF and 420 μm SMF, and Fig. 4(b) depicts its cross-section. The error in the structural length is within the acceptable range of the sensor design, and there are grinding marks on the adjacent SMF sections, but they do not have a special impact on the formation of the subsequent Vernier effect. Then, NOA61 (Norland Products Inc.) is a type of UV-curable adhesive suitable for humidity and temperature

Optics EXPRESS

sensing [35,36]. An optical fiber needle (125 µm) is used to dip a small amount of liquid NOA61 and gently fill it into the C-shaped cavity, with the assistance of a microscope, to ensure no air bubbles form to compromise the vernier effect and adequate filling. Next, the sensor is exposed to approximately 270 mW/cm^2 of UV light for 15 minutes to cure the UV adhesive, and then placed in a dust-free box for 12 hours to allow the NOA61 to fully crosslink with the fiber walls. Figure 4(c) and (d) depict the magnified views of the C-shaped cavity before and after it was filled with the NOA 61, respectively.

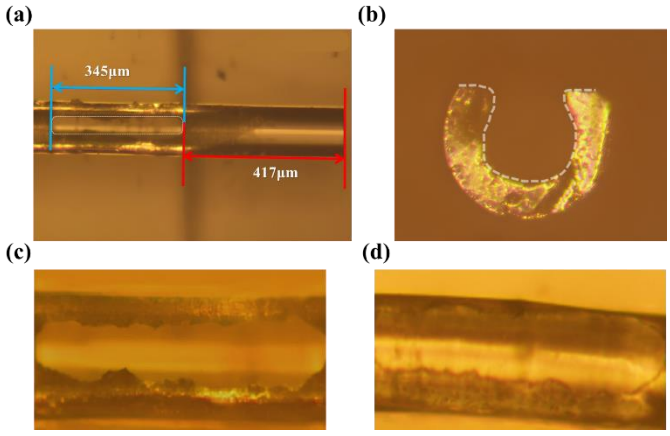

Fig. 4. (a) Image of the compact cascaded FP fiber structure. (b) Cross section of C-shaped cavity. (c), (d) Images of the C-shaped cavity before and after filling and curing with NOA61.

3. Experimental results and discussion

The RH and temperature performance testing system is depicted in Fig. 5. The system primarily comprises: the sensor; a broadband source (BBS, Lightcomm Co., ASE-C + L), operating wavelength range: 1525-1610 nm, output power ≥ 10 dBm; an optical spectrum analyzer (OSA, Japan Yokogawa, AQ6370), detection wavelength range: 600-1700nm, spectral resolution 0.02 nm, power range: -90 dBm to 20 dBm; an optical Circulator (OC), with an isolation of 50 dB; and a desktop constant temperature and humidity chamber (CTHC, J-TOPH-22-B, Jiexin Test Equipment Co., Ltd.), temperature detection range: -20 °C to 100 °C, relative humidity detection range: 30% RH to 95% RH, temperature accuracy: ± 0.3 °C, relative humidity accuracy: ± 2% RH. During subsequent experimental testing, the sensor is consistently positioned within the CTHC, and two plastic plugs are used to seal the CTHC to create a stable experimental environment. When the environmental values displayed by the CTHC reach the preset values, in order to ensure the stability of the sensor's environment and the spectrum, it is necessary to wait for 10 minutes (referred to as the waiting time) before proceeding with spectral scanning and recording.

After all the preparations were ready. Figure 6 presents the normalized spectral response of the sensor under 75% RH and 25°C. It is evident that the reflected spectrum of the sensor exhibits a standard vernier spectrum, with a prominent envelope curve that follows the FSR pattern. Consistent with the simulation in Section 2.2, the lower envelope, while exhibiting a high contrast, suffers from low optical intensity and susceptibility to interference, resulting in multiple uneven points and large fitting errors. Therefore, the upper envelope is more suitable for analyzing the sensor's sensitivity. After fitting and calculation, the actual Vernier envelope FSR of the sensor at 75% RH and 25 °C is about 20.8 nm and the fine internal fringes within this envelope is 1.0 nm. Furthermore, the refractive index of cured NOA 61 is 1.56, and the refractive index of single-mode optical fiber is 1.45. Using Eq. (7), the theoretical FSR of the envelope

Optics EXPRESS

can be calculated to be 20.2 nm, which is very close to the FSR obtained by fitting the vernier envelope in the experiment.

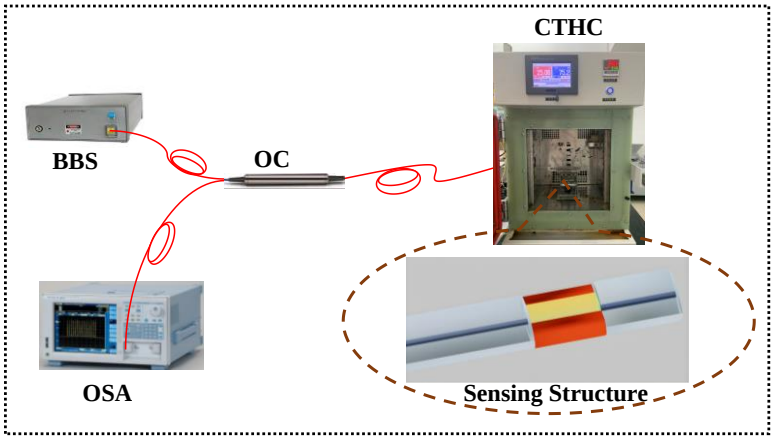

Fig. 5. RH and temperature performance testing system.

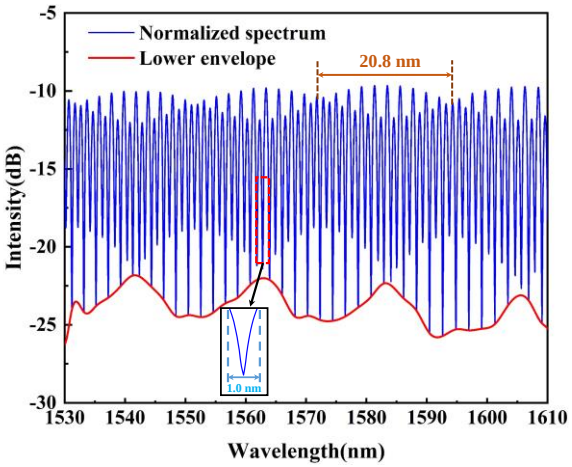

Fig. 6. Reflection spectrum of the sensor under 25°C with 75% RH.

3.1. Relative humidity measurement

In a controlled temperature environment of 25°C, the sensor spectral tests are conducted with a gradient of 10%RH for relative humidity increase and decrease within the relative humidity range of 35%RH to 95%RH. Figure 7 depicts the humidity-induced the upper vernier envelope changes. As humidity rises, the reflection spectrum envelope exhibits a red shift, whereas a blue shift is observed as humidity decreases. This spectral shift is attributed to the entry and exit of water molecules into the voids of the solidified NOA61 material, causing a corresponding increase or decrease in the effective refractive index of the NOA61. Next, a linear fitting is performed between humidity changes and the shift of the upper envelope, as shown in Fig. 8. Therefore, the envelope sensitivity $S_{envelope}$ for relative humidity is measured to be 0.248 nm/%RH in 35% - 95% RH.

Optics EXPRESS

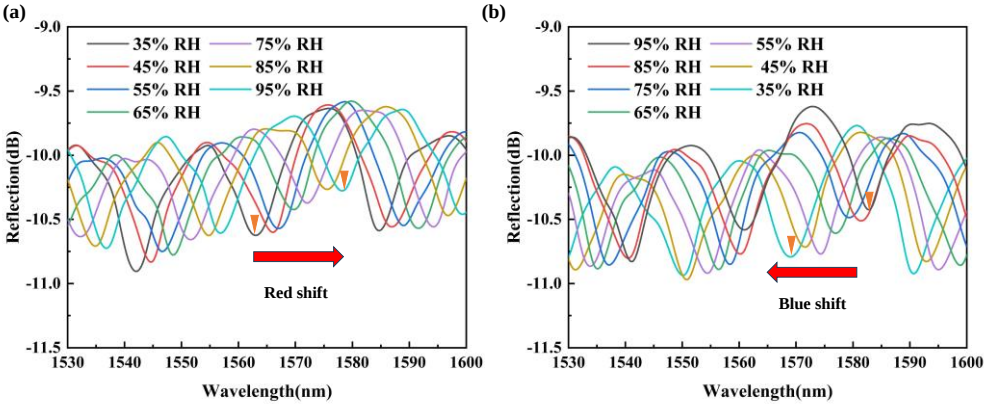

Fig. 7. Variation of the upper envelope trough's shift with temperature change. (a) Rising RH, 35%-95% RH. (b) Falling humidity, 35%-95% RH.

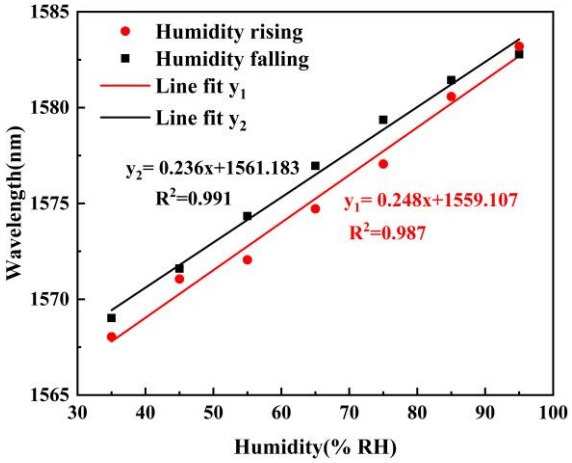

Fig. 8. Relationship between the shift of the upper envelope and the rise and fall of relative humidity.

3.2. *Temperature measurement*

Under the constant humidity condition of 70% RH, spectral tests were conducted on the sensor with temperature rising and falling in increments of 5°C within the range of 25°C to 65°C. Due to the large envelope shift, the temperature measurement experiments within the range of 25°C to 65°C were divided into two groups: 25°C to 45°C and 45°C to 65°C. Figure 9 shows the variation of the upper vernier envelope with temperature at 70% RH. It can be observed that, as the temperature rises, there is a regular blue shift in the upper envelope, and conversely, as the temperature falls, the envelope undergoes a red shift. This is due to the changes in the effective refractive index of the sensitive material (NOA 61), caused by its thermal expansion and thermo-optic effects, which result in a regular shift in the envelope.

At a constant 70% RH, a linear fitting process is performed on the upper envelope data with respect to temperature. As shown in Fig. 10, within the temperature range of 25 °C to 65 °C, the temperature sensitivity of the sensor is -1.091 nm/°C when the temperature rises, and -1.047 nm/°C when the temperature falls. The resolution of the sensor to temperature is about 0.02 °C. Then, Table 2 presents the comparison of the fabricated cascaded FP sensor

Optics EXPRESS

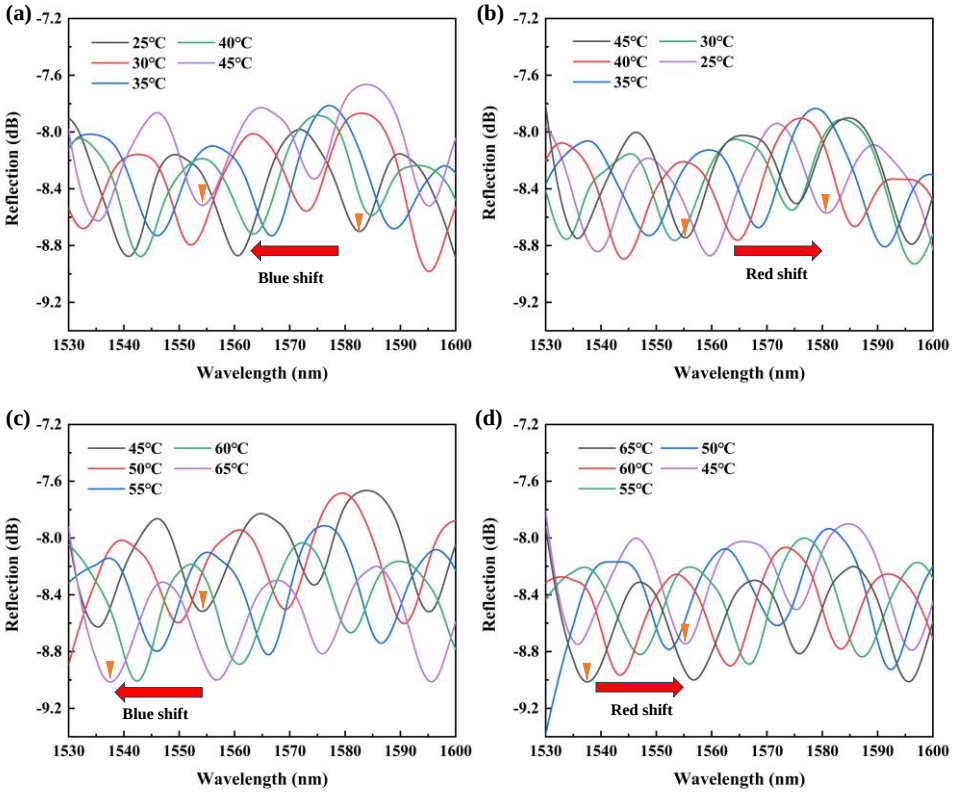

Fig. 9. Variation of the upper envelope trough's shift with temperature change. (a) Rising temperature, 25-45 °C. (b) Falling temperature, 25-45 °C. (c) Rising temperature, 45-65 °C. (d) Falling temperature, 45-65 °C.

with some recently reported single-structure sensors. Notably, traditional humidity-sensitive materials exhibit high hygroscopicity and expansibility, which tend to lead to hydrolysis in high humidity environments and desiccation shrinkage in low humidity environments. Therefore, they often perform poorly in real ambient conditions. However, NOA61, as a UV-curable adhesive, possesses the ability to resist oxidation and corrosion in complex environments.

3.3. RH and temperature compensation, response time, and stability

Given that analyzing the shift of the upper envelope trough alone exists the cross-interference of humidity and temperature, simultaneous detection of temperature and humidity can be achieved by further measuring the trough shift of the fine inner fringe within the envelope. Figure 11(a) shows how the trough of the fine inner fringe within the envelope shifts with humidity, and Fig. 11(b) presents a linear fit of the relationship between the trough shift and humidity. It can be observed that as RH rises, the trough undergoes a blue shift, which is in the opposite direction of the shift of the upper envelope trough. This aligns with the theoretical analysis presented in Section 2.1. Similarly, Fig. 11(c) and (d) demonstrate the relationship between the shift of the trough of the fine inner fringe and temperature. The sensitivity S_{fringe} of the inner fringe trough for relative humidity is 0.012 nm/%RH.

Therefore, the sensitivity of the trough of the inner fringe to humidity and temperature is -12.0 pm/%RH and -55.2 pm/°C respectively. Next, simultaneous detection of relative humidity and temperature can be achieved by performing a dual-parameter matrix operation on the sensor. The

Optics EXPRESS

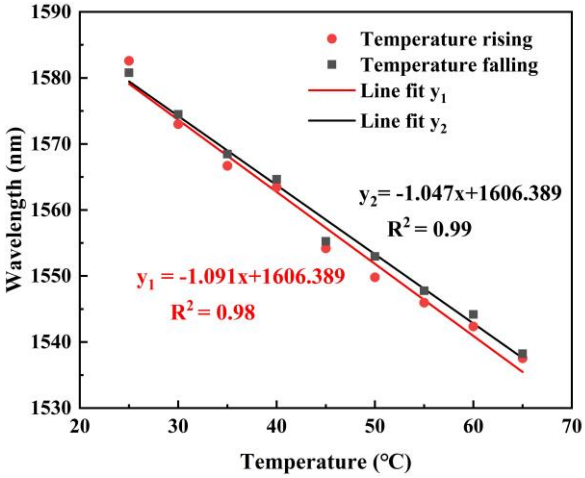

Fig. 10. Relationship between the shift of the upper envelope trough and the rise and fall of relative humidity.

Table 2. Comparison of optical fiber RH and temperature sensor performance

Reference	Fiber Structure	Sensing Material	RH range (RH%)	Sensitivity (nm/RH%)	Temperature range (°C)	Sensitivity (nm/°C)
[9]	MZI	PVA	30-95	0.256	20-80	0.153
[10]	MZI	PANI, GO	20-65, 65-85	0.020, 0.067	\	\
[36]	FBG, microsphere	NOA61	40-90	0.069	30-60	−0.11
[37]	FBG	Al_2O_3	11.3–84.3	0.185	30-55	0.01
[38]	FBG, FPI	None	40-90	0.348	25-70	-0.356
[20]	LPG	spider silks	50-80	-0.204	\	\
[39]	MI	Gelatin	45-81.7	-0.185	30-80	0.048
[13]	FPI	PDMS, PVA	20-45	-0.128, 0.038	20-45	0.022, -0.722
[15]	FPI	Chitosan, NOA 170, NOA 1315	50–85	0.437	26-46	0.29
This work	FPI	NOA61	35-95	0.248	25-65	-1.091

dual-parameter matrix can be expressed as:

$$\begin{bmatrix} \Delta\lambda_V \\ \Delta\lambda_F \end{bmatrix} = \begin{bmatrix} K_{V,H} & K_{V,T} \\ K_{F,H} & K_{F,T} \end{bmatrix} \begin{bmatrix} \Delta H \\ \Delta T \end{bmatrix} \tag{12}$$

$\Delta\lambda_V$ and $\Delta\lambda_F$ represent the wavelength shift of the upper envelope trough and the fine inner fringe trough respectively. $K_{V,H}$, $K_{V,T}$, $K_{F,H}$ and $K_{F,T}$ are the sensitivity coefficients of the envelope trough and the fine inner fringe trough to RH and temperature changes. Finally, ΔH and ΔT can be determined through matrix inversion:

$$\begin{bmatrix} \Delta H \\ \Delta T \end{bmatrix} = \begin{bmatrix} 0.248 & 0.012 \\ -1.091 & 0.0552 \end{bmatrix}^{-1} \begin{bmatrix} \Delta\lambda_V \\ \Delta\lambda_F \end{bmatrix} \tag{13}$$

Optics EXPRESS

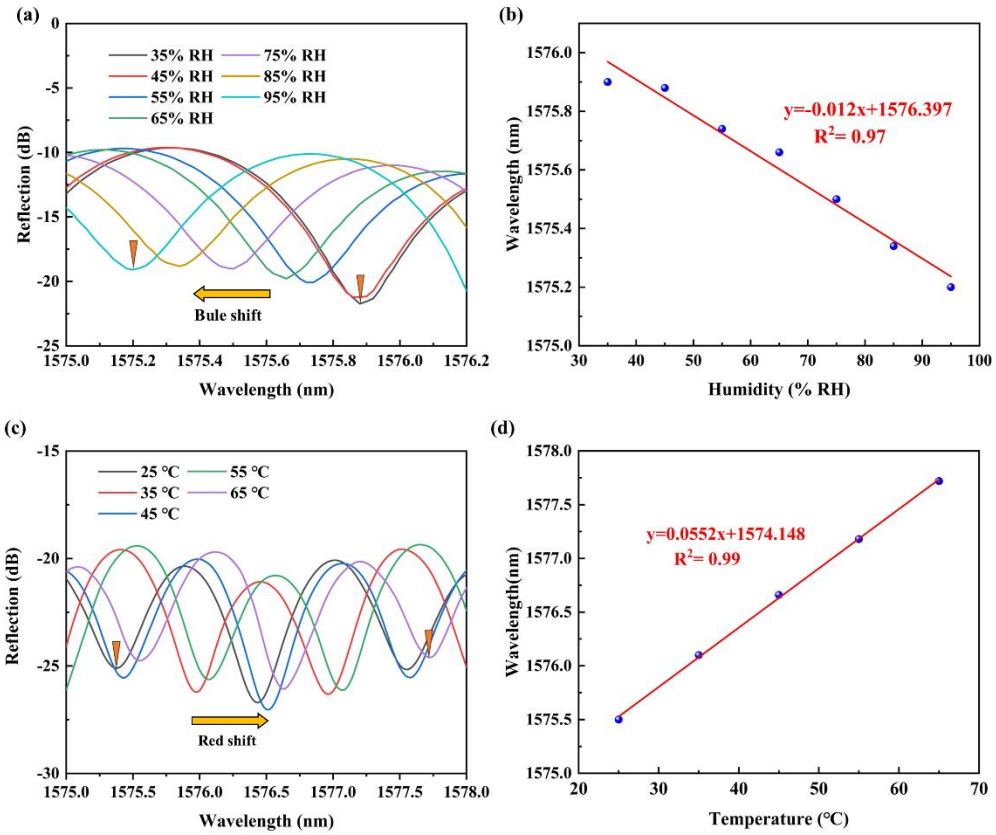

Fig. 11. (a) Shift of fine inner fringe trough with humidity; (b) Linear fit of trough shift and humidity; (c) Shift with temperature; (d) Linear fit of trough shift and temperature.

Response time reflects the sensor's ability for real-time environmental monitoring. The laboratory environment was measured to be 25 °C and 63%RH Using an electronic instrument. Therefore, the CTHC is set to 25 °C and 50%RH to test the response time to humidity changes, and to 30 °C and 63%RH to test the response time to temperature changes. The OSA automatically samples every 30s, and the change in the upper envelope trough over time is displayed in Fig. 12. It can be observed that within the range of 50%RH to 63%RH, the humidity response time (T_r) and recovery time (T_f) of the sensor are approximately 300s and 270s respectively. Similarly, within the temperature range of 25°C to 30°C, the temperature response time (T_r) and recovery time (T_f) of the sensor are approximately 210s and 240s respectively

The stability of optical fiber sensors serves as a pivotal metric, encapsulating their precision and consistency in practical applications. The sensor is placed in a sealed environment with 70% RH and 25°C, and its spectrum is recorded every 20 minutes over a period of 2 hours. The stability of the sensor is assessed by analyzing the position of the upper envelope's trough. The measurement results are shown in Fig. 13. It is evident that the experimental data closely correspond to the reference values over a period of two hours (with a standard deviation of 0.23). The minimal deviations demonstrate the reliable stability of the sensor.

Optics EXPRESS

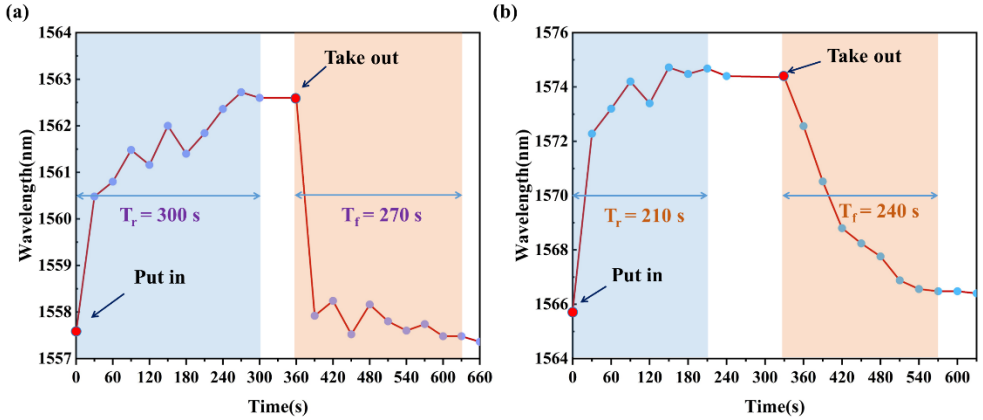

Fig. 12. (a) RH response and recovery times. (b) Temperature response and recovery times.

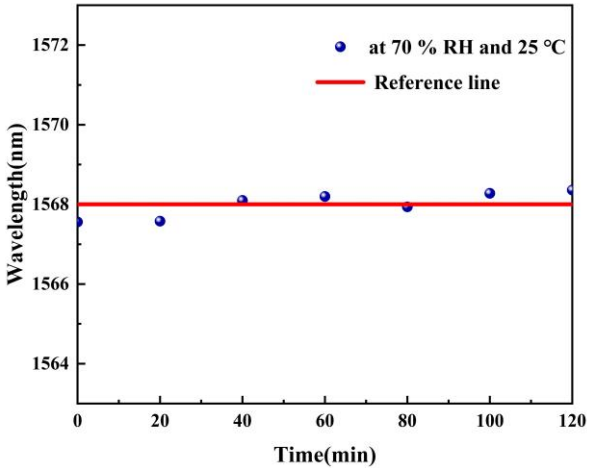

Fig. 13. Stability testing of the sensor.

4. Conclusion

In conclusion, we propose a novel cascaded FPI sensing structure based on a C-shaped cavity. This C-shaped cavity is simply created by grinding a hollow-core fiber using fiber optic abrasive paper, thus eliminating the need for complicated operations and expensive manufacturing costs. Furthermore, the C-shaped cavity filled with NOA61 and the attached single-mode fiber pigtail create three FPI structures: two short and one long. This configuration facilitates the development of a compact FPI relative humidity and temperature sensor that ingeniously leverages the optical Vernier effect to enhance sensor sensitivity. Finally, the proposed RH and temperature sensor achieves a RH sensitivity of 0.248 nm/%RH within the range of 35-95%RH, and a temperature sensitivity of -1.091 nm/°C within the range of 25 - 65°C, respectively. Additionally, the response time and recovery time of the sensor for RH and temperature are both within 300s, and the simultaneous measurement of RH and temperature can be achieved through the establishment of a dual-parameter matrix. Notably, the proposed sensor can effectively address detachment of the water-absorbing sensing membrane that coats the surface of traditional optical fiber humidity sensors. Simultaneously, compared to traditional humidity-sensitive materials, NOA61, as a UV

Optics EXPRESS

curing adhesive, possesses strong antioxidant and corrosion-resistant properties. Overall, the proposed sensor holds significant practical application value.

Funding. National Natural Science Foundation of China (61935007, 62075247, 62105379, U22A2087); The Special Project for Marine Economy Development of Guangdong Province (Six Marine Industries) under Department of Natural Resources of Guangdong Province(GDNRC [2024]16); Technical Support for Nature Gas Hydrate Drilling (DD20230066); Deep Sea Science and Engineering Technology Experiment (DD20242659).

Disclosures. The authors declare no conflicts of interest.

Data Availability. Data underlying the results presented in this paper are not publicly available at this time but may be obtained from the authors upon reasonable request.

References

1. S. Xinli, Z. Neng, and Z. Guozhong, "The combined effect of temperature, relative humidity and work intensity on human strain in hot and humid environments," Build. Environ. **69**, 72–80 (2013).
2. L. Baizhan, D. Chenqiu, T. Meilan, *et al.*, "A modified method of evaluating the impact of air humidity on human acceptable air temperatures in hot-humid environments," Energy Build. **158**, 393–405 (2018).
3. X. Chang, Z. Xin, and S. Shifei, "A numerical study of the effects of ambient temperature and humidity on the particle growth and deposition in the human airway," Environ. Res. **200**, 111751 (2021).
4. C. Huang, M. Jiang, and F. Liu, "Recent progress on environmentally friendly humidity sensor: a mini review," ACS Appl. Electron. Mater. **5**(8), 4067–4079 (2023).
5. K. Wu, H. Zhang, Y. Chen, *et al.*, "All-silicon microdisplay using efficient hot-carrier electroluminescence in standard 0.18μm CMOS technology," IEEE Electron Device Lett. **42**(4), 541–544 (2021).
6. Y. Guofeng, W. Delin, J. U. Long, *et al.*, "High-performance towing cable hydrophone array with an improved ultra-sensitive fiber-optic distributed acoustic sensing system," Opt. Express **31**(16), 25545–25556 (2023).
7. Z. L. Ke Zhao, L. Liu, C. Yu, *et al.*, "Functionalized reflective structure fiber-optic interferometric sensor for trace detection of lead ions," Acta Phys. -Chim. Sin. **40**(4), 2304029 (2023).
8. Z. Wang, Z. Chen, L. Ma, *et al.*, "Optical microfiber intelligent sensor: wearable cardiorespiratory and behavior monitoring with a flexible wave-shaped polymer optical microfiber," ACS Appl. Mater. Interfaces **16**(7), 8333–8345 (2024).
9. Z. Dong, Y. Jin, G. Zhang, *et al.*, "Single core-offset Mach-Zehnder interferometer coated with PVA for simultaneous measurement of relative humidity and temperature," Opt. Express **29**(15), 24102–24117 (2021).
10. X. Huang, S. Wang, J. Xie, *et al.*, "A novel polyaniline/graphene oxide composite film coated humidity sensor based on a Mach-Zehnder interferometer with thin-core fiber," IEEE Sens. J. **24**(13), 20629–20637 (2024).
11. M. Shao, R. Zhang, X. Zhao, *et al.*, "Dual-core fiber based in-line Michelson interferometer for humidity sensing," Opt. Fiber Technol. **64**, 102570 (2021).
12. B. Xu, Y. Guo, X. Ma, *et al.*, "Highly sensitive fiber relative humidity sensor based on tip Michelson interferometer with agarose gel coating," IEEE Sens. J. **23**(2), 1139–1145 (2023).
13. F. Li, X. G. Li, X. Zhou, *et al.*, "Simultaneous measurement of temperature and relative humidity using cascaded c-shaped Fabry-Perot interferometers," J. Lightwave Technol. **40**(4), 1209–1215 (2022).
14. J. Wang, Y. Kou, A. Wang, *et al.*, "Lab-on-fiber: laser-induced micro-cavity for a relative humidity measurement," Opt. Lett. **48**(20), 5261–5264 (2023).
15. Y. Wang, W. Yuan, Y. Yan, *et al.*, "Signal processing integrated with fiber-optic Vernier effect for the simultaneous measurement of relative humidity and temperature," Opt. Express **31**(17), 28636–28648 (2023).
16. H. Fan and H. Fan, "Sagnac interferometer embedded with fiber Bragg grating for relative humidity and temperature sensing," Opt. Commun. **569**, 130802 (2024).
17. Y. Liu, H. Gong, X. Lu, *et al.*, "Fiber Bragg grating humidity sensor based on side-polished step-index multimode fiber coated with GO," Opt. Laser Technol. **177**, 111175 (2024).
18. H. Wang, S. Gao, X. Yue, *et al.*, "Humidity-sensitive PMMA fiber Bragg grating sensor probe for soil temperature and moisture measurement based on its intrinsic water affinity," Sensors **21**(21), 6946 (2021).
19. A. Pospori, C. A. F. Marques, O. Bang, *et al.*, "Polymer optical fiber Bragg grating inscription with a single UV laser pulse," Opt. Express **25**(8), 9028–9038 (2017).
20. Y. Zhang, J. Yang, M. Zhang, *et al.*, "Long-period fiber grating humidity sensor based on spider silks," Sens. Actuators, A **342**, 113660 (2022).
21. H. Guo, Y. Ning, Y. Zhang, *et al.*, "Wearable fiber SPR respiration sensor based on a LiBr-doped silk fibroin film," ACS Sens. **8**(11), 4171–4178 (2023).
22. A. G. Leal-Junior and C. Marques, "Diaphragm-embedded optical fiber sensors: a review and tutorial," IEEE Sens. J. **21**(11), 12719–12733 (2021).
23. T. Chen, H. Jiang, H. Xia, *et al.*, "U-shaped microfiber sensor coated with PVA nanofibers for the simultaneous measurement of humidity and temperature," Sens. Actuators, B **378**, 133203 (2023).
24. Y. Liu, X. Li, Y. N. Zhang, *et al.*, "Fiber-optic sensors based on Vernier effect," Measurement **167**, 108451 (2021).
25. R. J. Tong, B. Xing, Z. H. Chen, *et al.*, "High-Sensitivity Fiber Optic Temperature Sensor Based on Enhanced Vernier Effect," IEEE Trans. Instrum. Meas. **73**, 1–8 (2024).

Optics EXPRESS

26. Y. Li, Y. Li, Y. Liu, *et al.*, "Detection limit analysis of optical fiber sensors based on interferometers with the Vernier-effect," Opt. Express **30**(20), 35734–35748 (2022).
27. L. Zhao, S. Hao, Y. Chen, *et al.*, "Simultaneous measurement of strain and temperature based on fiber sensor with Vernier effect," Opt. Laser Technol. **157**, 108670 (2023).
28. C. Yu, H. Gong, Z. Zhang, *et al.*, "Temperature-compensated high-sensitivity relative humidity sensor based on band-pass filtering and Vernier effect," IEEE Trans. Instrum. Meas. **71**, 1–8 (2022).
29. Y. L. Yuan, R. J. Tong, B. Xing, *et al.*, "Cascaded Vernier effect optic fiber temperature sensor with DSHF-Based MZI and FPI," Measurement **231**, 114625 (2024).
30. T. Zhang, Q. Han, Z. Liang, *et al.*, "A Fabry–Perot sensor with cascaded polymer films based on vernier effect for simultaneous measurement of relative humidity and temperature," Sensors **23**(5), 2800 (2023).
31. Y. Zhao, X. X. Wang, R. Q. Lv, *et al.*, "Highly sensitive reflective Fabry–Perot magnetic field sensor using magnetic fluid based on Vernier effect," IEEE Trans. Instrum. Meas. **70**, 1–8 (2021).
32. K. J. J. O. M. Xu, "Silicon electro-optic micro-modulator fabricated in standard CMOS technology as components for all silicon monolithic integrated optoelectronic systems," J. Micromech. Microeng. **31**(5), 054001 (2021).
33. F. Li, X. Li, X. Zhou, *et al.*, "Plug-in label-free optical fiber DNA hybridization sensor based on C-type fiber Vernier effect," Sens. Actuators, B **354**, 131212 (2022).
34. H. Zheng, R. Lv, Y. Zhao, *et al.*, "Multifunctional optical fiber sensor for simultaneous measurement of temperature and salinity," Opt. Lett. **45**(24), 6631–6634 (2020).
35. C. L. Lee, C.-S. Chen, C.-R. Yang, *et al.*, "NOA61-polymer fiber Fizeau interferometer with a flexible NOA65-polymer taper for simultaneous measurement of tilt angle and temperature," in *Polymers*, (2021).
36. H. Fan, Y. Sun, Y. Bao, *et al.*, "Polymer microsphere integrated with fiber Bragg grating for simultaneous monitoring of relative humidity and temperature," Measurement **225**, 113990 (2024).
37. J. Peng, J. Zhou, C. Sun, *et al.*, "Optical fiber temperature and humidity dual parameter sensing based on fiber Bragg gratings and porous film," Sensors **23**(17), 7587 (2023).
38. D. Liu, Z. Cai, B. Li, *et al.*, "Simultaneous measurement of humidity and temperature based on fiber-tip microcantilever cascaded with fiber Bragg grating," Opt. Express **31**(5), 8738–8747 (2023).
39. Y. Liu, A. Zhou, and L. Yuan, "Gelatin-coated Michelson interferometric humidity sensor based on a multicore fiber with helical structure," J. Lightwave Technol. **37**(10), 2452–2457 (2019).